ACS Photonics

pubs.acs.org/journal/apchd5

Article

Silicon Quantum Dot Luminescent Solar Concentrators and Downshifters with Antireflection Coatings for Enhancing Perovskite Solar Cell Performance

Shuzhen Ren, Chunhui Shou, Shengli Jin, Guo Chen, Shanshan Han, Zongqi Chen, Xinyu Chen, Songwang Yang,* Yunlong Guo,* and Chang-Ching Tu*

Cite This: *ACS Photonics* 2021, 8, 2392–2399

Read Online

ACCESS | Metrics & More | Article Recommendations | Supporting Information

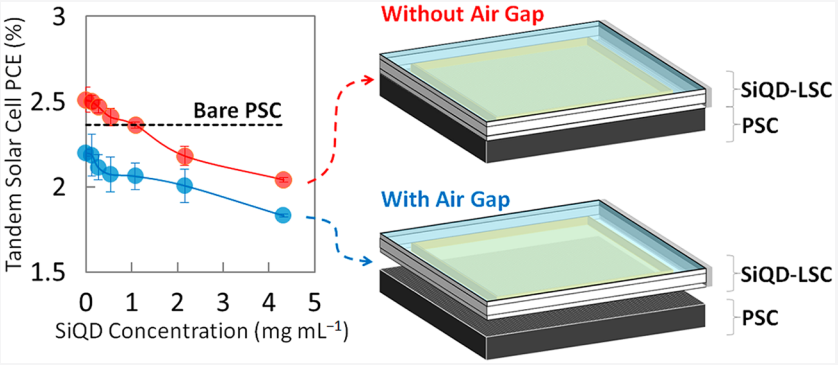

ABSTRACT: In this work, we demonstrate a four-terminal tandem solar cell consisting of a luminescent solar concentrator (LSC) based on silicon quantum dots (SiQDs) in front of a 4 cm × 4 cm perovskite solar cell (PSC). The LSC front surface is uniformly covered with a nanoporous poly(methyl methacrylate) (PMMA) antireflection coating, which can enhance the transmission by up to 3% from the visible to the near-infrared range. The colloidal SiQDs inside the LSC primarily absorb the UV portion of the solar irradiation, re-emitting red fluorescence, which propagates to the waveguide edges for generating electricity while allowing the rest of the incident sunlight to be absorbed in the back PSC. With an air gap between the SiQD-LSC and PSC, compared to the bare PSC, the two devices in combination exhibits significant external quantum efficiency (EQE) enhancement under 365 nm UV illumination, but shows no power conversion efficiency (PCE) enhancement under xenon arc lamp illumination. In contrast, when the air gap is removed, the SiQD-LSC becomes a luminescent downshifter than a concentrator, with most of the SiQD fluorescence being absorbed by the back PSC. In this case, the SiQD-LSC/PSC tandem solar cell can achieve up to 6.2% PCE enhancement over the bare PSC at low SiQD concentrations. Particularly, at 1.08 mg mL^{-1}, although the tandem solar cell has about the same PCE as the bare PSC, the front SiQD-LSC absorbs 69% of the solar UV, making the back PSC more stable than the bare PSC.

KEYWORDS: *silicon quantum dots, luminescent solar concentrators, downshifters, antireflection coatings, perovskite solar cells*

Solution-processable organometal halide perovskite solar cells (PSCs) have recently made tremendous progress in achieving high power conversion efficiencies (PCEs), improving from 3.8% in 2009 to 25.5% in 2021,[1,2] while showing the potential to be far less expensive to manufacture compared to conventional crystalline silicon solar cells.[3,4] Despite the high efficiency and low manufacturing cost, the relatively short device lifetime has been one of the most critical issues of PSCs to be resolved before commercialization.[5] Such device instability could result from intrinsic factors, such as ion migration,[6] and extrinsic factors, such as moisture,[7] heat,[8] and UV exposure.[9,10] In addition to strengthening the intrinsic stability at the material and device architecture levels,[11−13] encapsulation is another cost-effective way to insulate the device from those detrimental factors from the outside.[14,15]

As an additive layer to the encapsulation, a luminescent downshifter is often employed to convert the UV part of the solar irradiation into visible light, which is less harmful to and better utilized by the PSCs. Such stability enhancement is particularly significant for the PSCs with titanium dioxide electron transport layers, which upon UV irradiation may suffer from the photocatalytic recombination at the titanium dioxide/

Received: April 11, 2021
Published: August 9, 2021

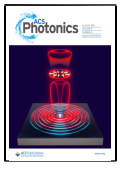

https://doi.org/10.1021/acsphotonics.1c00550
ACS Photonics 2021, 8, 2392–2399

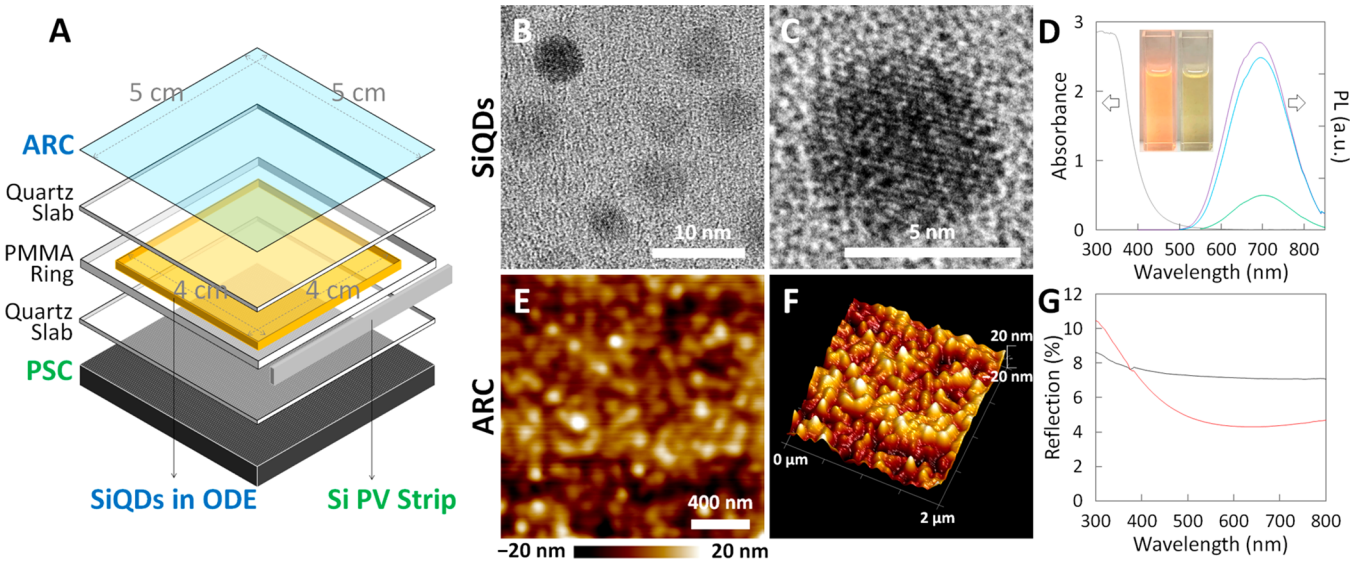

Figure 1. (A) Expanded 3D view of the SiQD-LSC, consisting of a front quartz slab (1 mm thick), a PMMA ring (2 mm thick), and a rear quartz slab (1 mm thick). The void structure formed by the two quartz slabs and the PMMA ring is filled with the SiQD suspension in ODE. Besides, the airside surface of the front quartz slab has a nanoporous PMMA ARC. Here the two PV components, a PSC and a Si PV strip, are located at the back and edge of the SiQD-LSC, respectively. (B, C) TEM images of the SiQDs. (D) Absorption (gray line) and PL spectra of the SiQD suspension in ODE (1.08 mg mL^{-1}), with 365 (purple line), 465 (blue line), and 525 nm (green line) excitation. The inset shows the photographs of the SiQD suspension under 365 nm UV light (left) and white light (right) illumination. (E, F) AFM images of the nanoporous PMMA ARC. (G) Reflection spectra of the bare quartz slab (black line) and the quartz slab having the nanoporous PMMA ARC (red line).

perovskite interface. In general, the luminescent downshifting materials should possess strong UV absorption and efficient visible emission. For example, europium-doped rare earth phosphors with selective absorption in the UV range were coated on the nonconducting surface of the fluorine-doped tin oxide (FTO) glass of the PSC for reducing the UV degradation, while achieving more than 15% higher PCEs owing to the downshifting.[16,17] On the other hand, fluorescent carbon dots and lanthanide-containing polyoxometalates were incorporated in the mesoporous titanium dioxide layers of the PSCs, which also leads to obvious enhancement of the stability and efficiency.[18,19]

Besides luminescent downshifters, antireflection coatings (ARCs) have also been applied to mitigate the reflection loss. In general, the ARCs for conventional silicon solar cells include the silicon nitride coating applied over the textured Si surface and inorganic materials, such as SiO_2, MgF_2, and TiO_2, deposited on the module glass surface.[20−22] Without such ARCs, the overall optical loss can be as high as 35−36%.[23] For the PSCs, considering the perovskite layers are relatively vulnerable to microfabrication techniques for texturing, the ARCs are primarily applied to the cover glass surfaces. For example, disordered micropyramids made of polydimethylsiloxane (PDMS) polymer were coated on the nonconducting surface of the FTO glass of the PSC, leading to a 1.6-fold absorption enhancement, with the electrical properties of the PSC kept almost unchanged.[24]

Another way to alleviate the UV degradation while also improving the efficiency is the use of tandem architecture, in which the front solar cell absorbs the shorter wavelengths of the solar spectrum, allowing the longer wavelengths to be absorbed by the back solar cell. Recently, various perovskite-based tandem solar cells, mainly perovskite/silicon, perovskite/CIGS, and perovskite/perovskite, have demonstrated that they can achieve higher PCEs than their standalone subcells.[25,26] On the other hand, other bandgap-tunable optical devices that could potentially work as the front solar cells in tandem with PSCs are yet to be explored. In this work, we demonstrate a four-terminal tandem solar cell consisting of a luminescent solar concentrator based on colloidal silicon quantum dots (SiQD-LSC) in front of a PSC. The front surface of the SiQD-LSC is uniformly covered with a nanoporous poly(methyl methacrylate) (PMMA) ARC for reducing the reflection loss at the air/quartz interface. The SiQD suspension sandwiched between two thin quartz slabs primarily absorbs the UV portion of the solar irradiation, re-emitting red fluorescence, which propagates across the planar waveguiding structure to the edges, where the concentrated red fluorescence is converted to electricity by conventional Si PV strips. After passing through the SiQD-LSC, which absorbs the UV part, the rest of the incident sunlight is absorbed by the back PSC.

When the air gap between the SiQD-LSC and PSC is removed, the refracting medium surrounding the SiQD-LSC is not thoroughly air and, thus, the waveguiding ability of the SiQD-LSC diminishes significantly. In this case, the SiQD-LSC functions like a luminescent downshifter than a concentrator, with the majority of the SiQD fluorescence being absorbed by the back PSC instead of the peripheral Si PV strips at the LSC edges. The main focus of this work is systematically investigating the performance of the SiQD-LSC/PSC four-terminal tandem solar cell with the nanoporous PMMA ARC, under the condition with or without an air gap between the two parts, which determines whether the role of the SiQD-LSC is a luminescent concentrator or a downshifter.

EXPERIMENTAL RESULTS

Fabrication and Characterization of the SiQD-LSCs. The SiQD-LSC consists of a front quartz slab, a PMMA ring, and a rear quartz slab (Figure 1A). Both the front and rear quartz slabs are 1 mm thick, while the PMMA ring is 2 mm thick. The void structure formed by the two quartz slabs and the PMMA ring is filled with the SiQD suspension, and the

https://doi.org/10.1021/acsphotonics.1c00550
ACS Photonics 2021, 8, 2392−2399

airside surface of the front quartz slab has a nanoporous PMMA ARC. The synthesis of the SiQDs was based on a top-down method developed previously,[27] briefly described as follows. A p-type crystalline silicon wafer was electrochemically etched in an electrolyte containing hydrofluoric acid and methanol, followed by a white-light induced hydrosilylation reaction with 1-octene for surface passivation. The resulting porous silicon layer along with the 1-octene was harvested from the wafer surface and then transferred to a zirconia milling jar for high energy ball milling. Finally, the mixture was centrifuged to precipitate the agglomeration of large particles, while the monodisperse, 1-octene passivated SiQDs were collected in the supernatant. According to the transmission electron microscopy (TEM) images (Figure 1B,C), overall the SiQDs have round shapes and particle sizes less than 5 nm. From the fast Fourier transform (FFT) electron diffraction pattern and the interplanar spacing, it is confirmed that the SiQDs are constituted of crystalline silicon (Supporting Information, Figure S1). Passivated with the 1-octene ligands,[27] the SiQDs can form uniform and stable suspension in various nonpolar organic solvents, such as toluene, hexane, and 1-octadecene (ODE). In this work, the SiQD suspension in ODE is very stable, without any precipitates observed for months. The main absorption of the SiQD suspension in ODE lies in the UV range, in addition to the weak visible absorption from 400 to 500 nm (gray line in Figure 1D). Owing to the minor blue absorption, the SiQD suspension appears light yellow in color under white light (right inset in Figure 1D). Under 365 nm excitation (purple line and left inset in Figure 1D), the SiQD suspension emits bright red fluorescence with the peak wavelength located at 690 nm and the photoluminescence quantum efficiency (PLQY) equal to 38.86% (Supporting Information, Figure S2). Furthermore, the PL peak wavelength remains almost unchanged when the excitation wavelength was changed to 465 and 525 nm (blue and green lines in Figure 1D). Most importantly, the overlap between the absorption and emission spectra is small, which is beneficial for suppressing the reabsorption effect of the SiQD fluorescence.

The nanoporous PMMA ARC was fabricated by a microphase separation method.[28] First, a mixture of PMMA (M_w = 15 kg mol^{-1}) and polystyrene (PS, M_w = 14 kg mol^{-1}) with 4:6 weight ratio was uniformly dissolved in chloroform to yield a 1 wt % solution, which was then spin-coated on a piranha-cleaned quartz slab. The PMMA/PS coated quartz slab was sequentially dried and annealed in a vacuum oven at 50 °C for 10 h and 110 °C for 10 min, followed by soaking in cyclohexane which dissolves the PS component, leaving only the nanoporous PMMA film on the substrate. Finally, after rinsed with deionized water and dried with nitrogen stream, the quartz slab with the nanoporous PMMA ARC is used for constructing the SiQD-LSC. According to the atomic force microscopy (AFM) images (Figure 1E,F), the PMMA film is characterized with larger pore sizes at the top and smaller pore sizes at the bottom, resulting in an effective refractive index between 1.2 and 1.3 from 300 to 800 nm, measured by an ellipsometry method (Supporting Information, Figure S3). Compared to the bare quartz slab, the quartz slab having the nanoporous PMMA ARC exhibits significantly lower reflection, with the reflection decreasing from 7.64% to 6.97%, from 7.15% to 4.33% and from 7.07% to 4.68% at 400, 600, and 800 nm, respectively (Figure 1G).

Optical Properties of the SiQD-LSCs. The transmission spectra of the SiQD-LSC filled with the SiQD suspension in different concentrations are characterized (Figure 2A,B).

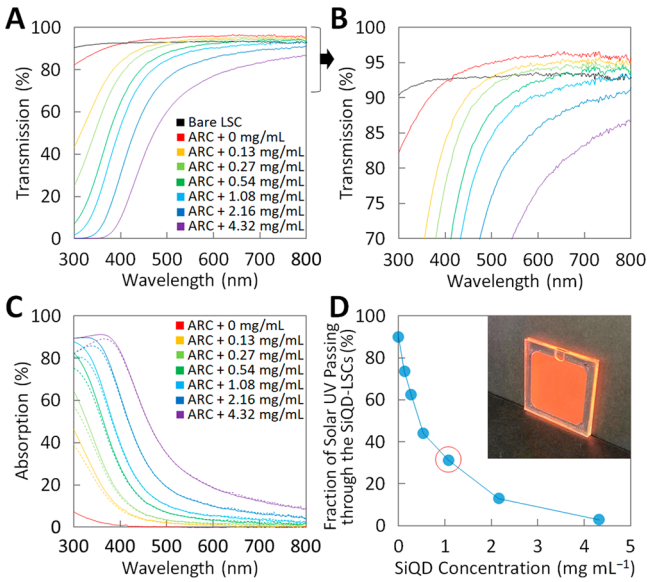

Figure 2. (A, B) Transmission spectra of the bare LSC and the SiQD-LSC with different SiQD concentrations. (C) Absorption spectra of the SiQD-LSC (solid lines) and the SiQDs alone (dashed lines) with different SiQD concentrations. (D) Fractions of the solar UV, the 300-to-400 nm part of the AM1.5G solar spectrum, passing through the SiQD-LSC with different SiQD concentrations. The inset shows the photograph of the SiQD-LSC (1.08 mg mL^{-1}) under 365 nm UV illumination.

Compared to the bare LSC having neither SiQD nor the nanoporous PMMA ARC (black line), just the addition of the ARC (red line) can improve the transmission by up to 3% from 400 to 800 nm. When the SiQD concentration is increased to 0.13 (orange line) and 0.27 mg mL^{-1} (light green line), the UV-to-blue wavelength range transmission drops significantly due to the SiQD absorption, while the green-to-near-infrared wavelength range transmission still maintains higher than the bare LSC. When the SiQD concentration is further increased to 0.54 (green line), 1.08 (light blue line), 2.16 (blue line), and 4.32 mg mL^{-1} (purple line), the transmission at nearly all wavelengths becomes lower than the bare LSC. Although the transmission enhancement due to the ARC is consumed by the SiQD absorption especially at high SiQD concentrations, the absorbed light is downshifted to red fluorescence which can be utilized by both the PSC and Si PV strip, located at the back and edge of the SiQD-LSC, respectively.

The absorption spectra of the SiQD-LSC with different SiQD concentrations (solid lines in Figure 2C) are obtained by one subtracted by the corresponding transmission spectra (Figure 2A) and reflection spectrum (red line in Figure 1G). In contrast, the absorption spectra of the SiQDs alone (dashed lines in Figure 2C) can be obtained by subtracting the transmission spectra of the SiQD-LSC with different SiQD concentrations from the transmission spectrum of the zero-concentration SiQD-LSC. For example, the absorption spectrum of the SiQDs with the concentration equal to 1.08 mg mL^{-1} (light blue dashed line in Figure 2C) is obtained by subtracting the transmission spectrum of the 1.08 mg mL^{-1}

https://doi.org/10.1021/acsphotonics.1c00550
ACS Photonics 2021, 8, 2392−2399

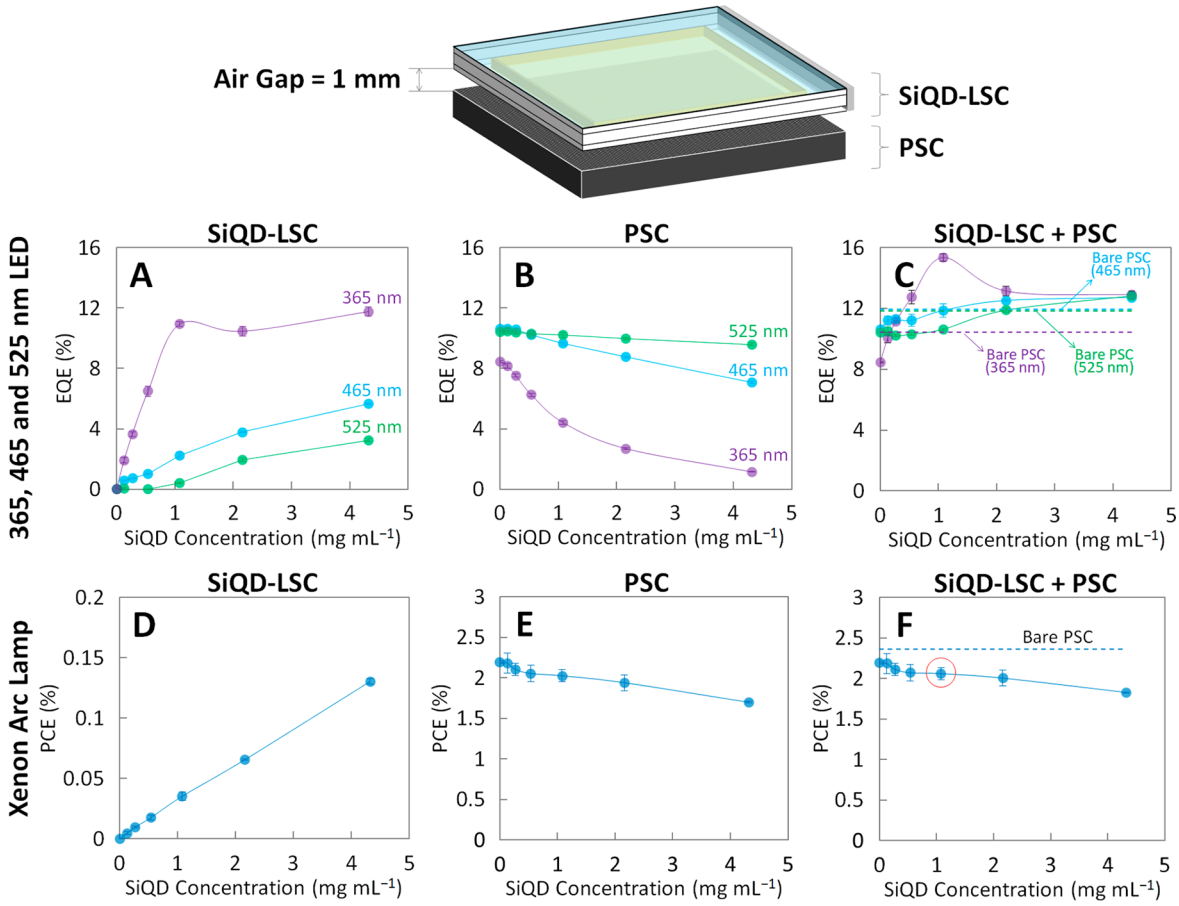

Figure 3. With a 1 mm air gap between the SiQD-LSC and PSC. (A–C) EQEs of the front SiQD-LSC, the back PSC and the combination of both under 365 (2.214 mW cm^{-2}), 465 (2.207 mW cm^{-2}), and 525 nm (2.212 mW cm^{-2}) LED illumination. (D–F) PCEs of the front SiQD-LSC, the back PSC and the combination of both under xenon arc lamp (8.109 mW cm^{-2}) illumination. The light absorbing area is consistently 4 cm × 4 cm. The dashed lines in (C) represent the 365, 465, and 525 nm EQEs (=10.45%, 11.95%, and 11.84%, respectively) of the bare PSC. Here the EQE values of the bare PSC are lower than the conventional ones because the PSC has five subcells in series that, although providing larger open-circuit voltage, is relatively unfavorable for the extraction of photocurrent under the short-circuit condition (Supporting Information, Figure S6). The dashed line in (F) represents the PCE (=2.36%) of the bare PSC. The EQE and PCE values of the SiQD-LSC in (A) and (D) are offset by the zero-concentration values, so that the background luminescence was excluded and only the SiQD fluorescence is considered. The short-circuit currents used for calculating the EQEs and PCEs of the SiQD-LSC are equal to the short-circuit currents generated by the Si PV strip multiplied by four.

SiQD-LSC (light blue line in Figure 2A) from the transmission spectrum of the zero-concentration SiQD-LSC (red line in Figure 2A). As shown in Figure 2C, the absorption spectra of the SiQD-LSC and the SiQDs alone are almost identical for wavelengths above 400 nm, indicating that the absorption due to the ARC, two quartz slabs and ODE in total (red solid line in Figure 2C) is negligible in the visible-to-near-infrared wavelength range. Lastly, to understand the SiQD-LSC's ability to remove UV which can cause instability of the PSC at the back, the fraction of the UV part (300 to 400 nm) of the AM1.5G solar spectrum passing through the SiQD-LSC is calculated (Figure 2D and Supporting Information, Figure S4). As the SiQD concentration increases from 0 to 0.54 to 4.32 mg mL^{-1}, the fraction of the solar UV passing through the SiQD-LSC decreases from 90% to 44% to 3%. The solar UV absorbed by the SiQDs is downshifted to red fluorescence. Except the escape cone losses at the front and back surfaces of the SiQD-LSC, the majority of the red fluorescence propagates to the four edges of the SiQD-LSC (inset in Figure 2D).

PV Performance of the SiQD-LSC/PSC Tandem Solar Cells. In this work, the Si PV strip is employed for harvesting the SiQD fluorescence, while the PSC mainly absorbs the remaining solar irradiation passing through the SiQD-LSC (Figure 1A). The PSC consists of five subcells connected in series, each having a structure of FTO/TiO_2/ZrO_2/perovskite ($(5\text{-AVA})_x MA_{1-x} PbI_3$)/carbon (Supporting Information, Figure S5A–C). The PSC is encapsulated between two glass slabs by a ring of butyl rubber sealant, and the active area of the PSC is 4 cm × 4 cm. On the other hand, the Si PV strip, which is mechanically diced from a conventional monocrystalline silicon solar cell wafer, has a size of 7 cm × 1 cm. The *I*–*V* characteristics of the two PV devices were measured before coupling to the SiQD-LSC (Supporting Information, Figure S5D,E). It is worth mentioning that, to avoid the complication of parallel wiring, in the following experiments only one Si PV strip is attached to the SiQD-LSC edge and the total electricity generated by the SiQD-LSC is equal to that generated by the Si PV strip multiplied by four. In literature, a similar analysis approach has also been adopted.[29] Besides, during the external quantum efficiency (EQE) and PCE measurements, the light absorbing area is consistently 4 cm × 4 cm, and all other parts, except the light absorbing area, are totally shielded from the

https://doi.org/10.1021/acsphotonics.1c00550
ACS Photonics 2021, 8, 2392–2399

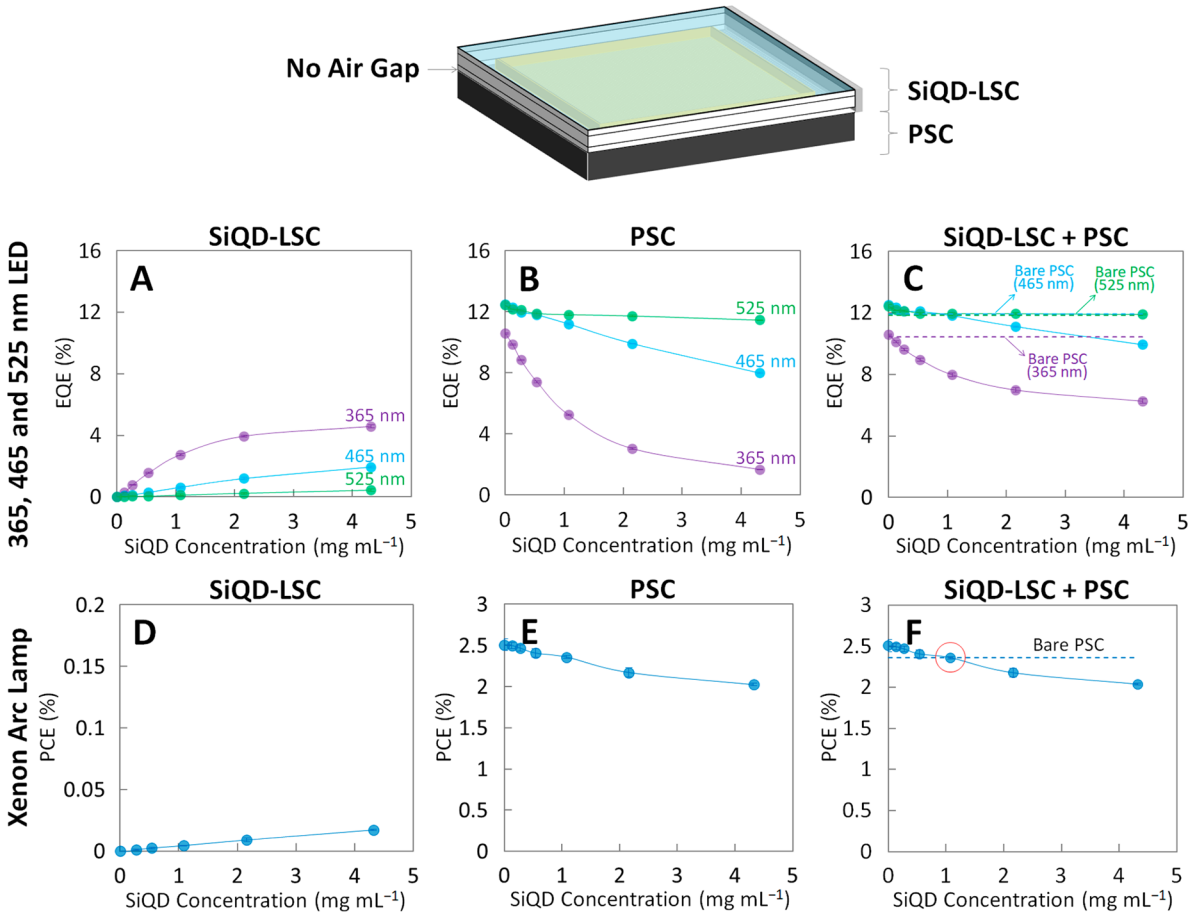

Figure 4. With no air gap between the SiQD-LSC and PSC. (A–C) EQEs of the front SiQD-LSC, the back PSC and the combination of both under 365 (2.214 mW cm^{-2}), 465 (2.207 mW cm^{-2}), and 525 nm (2.212 mW cm^{-2}) LED illumination. (D–F) PCEs of the front SiQD-LSC, the back PSC, and the combination of both under xenon arc lamp (8.109 mW cm^{-2}) illumination. The light absorbing area is consistently 4 cm × 4 cm. The dashed lines in (C) and (F) represent the 365, 465, and 525 nm EQEs (=10.45%, 11.95%, and 11.84%, respectively) and the PCE (=2.36%) of the bare PSC. The EQE and PCE values of the SiQD-LSC in (A) and (D) are offset by the zero-concentration values so that the background luminescence was excluded and only the SiQD fluorescence is considered. The short-circuit currents used for calculating the EQEs and PCEs of the SiQD-LSC are equal to the short-circuit currents generated by the Si PV strip multiplied by four.

light source. Particularly, except the edge attached to the Si PV strip and a small slot for loading the SiQD suspension, all other parts of the SiQD-LSC edges are closely attached with black tape to prevent the SiQD fluorescence from being reflected back into the LSC (Supporting Information, Figure S5F).

When there is a 1 mm air gap between the SiQD-LSC and PSC, the EQEs of the front SiQD-LSC, the back PSC and the combination of both under 365, 465, and 525 nm LED illumination are characterized. In the experiment, the short-circuit current of the SiQD-LSC with the PSC at the back and the short-circuit current of the PSC with the SiQD-LSC at the front were first measured individually, and then the sum of the two short-circuit currents corresponds to that of the SiQD-LSC/PSC tandem solar cell. The EQEs were calculated according to the measured short-circuit currents, the single-wavelength LED intensities and the light absorbing area (=4 cm × 4 cm). As the SiQD concentration increases from 0 to 4.32 mg mL^{-1}, the 365 nm EQE of the SiQD-LSC increases much faster than the 465 and 525 nm EQEs but reaches a plateau at 1.08 mg mL^{-1} (Figure 3A), which is attributed to the saturation of UV light absorption (Figure 2C) and the enhanced reabsorption effect at high SiQD concentrations. In contrast, with only part of the incident light passing through the SiQD-LSC, the EQE of the PSC decreases as the SiQD concentration increases (Figure 3B). Most importantly, the 365 nm EQE of the SiQD-LSC/PSC tandem solar cell is higher than the 365 nm EQE of the bare PSC for the SiQD concentrations higher than 0.27 mg mL^{-1}, with a peak value of 15.36% occurring at 1.08 mg mL^{-1}, which corresponds to a 47% enhancement over the bare PSC (Figure 3C). On the other hand, the 465 and 525 nm EQEs are generally lower than the bare PSC except at 2.16 and 4.32 mg mL^{-1}.

In addition to the analysis of EQEs which are based on the short-circuit currents measured by using single-wavelength LEDs, the PCEs of the front SiQD-LSC, the back PSC and the combination of both under the illumination of xenon arc lamp are also characterized. As the SiQD concentration increases from 0 to 4.32 mg mL^{-1}, the PCE of the SiQD-LSC linearly increases, improving from zero to 0.13% (Figure 3D), whereas the PCE of the PSC monotonically decreases, dropping from 2.20% to 1.70% (Figure 3E). Furthermore, the PCE of the SiQD-LSC/PSC tandem solar cell is lower than the bare PSC at all SiQD concentrations (Figure 3F). In summary, compared to the bare PSC, the SiQD-LSC/PSC tandem solar cell achieves higher EQEs at high SiQD concentrations but lower PCEs at all SiQD concentrations. This result can be explained by the fact that the PSC has five subcells in series, which is unfavorable for the extraction of photoexcited carriers under

https://doi.org/10.1021/acsphotonics.1c00550
ACS Photonics 2021, 8, 2392–2399

the short-circuit condition. In comparison, the short-circuit current of the SiQD-LSC is calculated by that of the Si PV strip multiplied by four, implying four Si PV strips connected in parallel. Therefore, the EQE increase due to the SiQD-LSC (Figure 3A) can overcome the EQE decrease due to the PSC (Figure 3B), particularly with the 365 nm illumination. However, when evaluating PCEs, both short-circuit currents and open-circuit voltages need to be taken into consideration. Given that the open-circuit voltages of the PSC with five subcells in series are much larger than the open-circuit voltages of the SiQD-LSC (Supporting Information, Table S1), the PCE decrease due to the PSC (Figure 3E) overwhelms the PCE increase due to the SiQD-LSC (Figure 3D).

The optical efficiency (η_{opt}) of the SiQD-LSC, defined as the percentage of the SiQD fluorescence photons being received by the Si PV strip, can be calculated by using the equation as follows, $\eta_{opt} = [4 \times \Delta I_{SC}/q/\text{Ø}_{PV}]/[I_{light} \times {W_{LSC}}^2 \times A_{SiQD}/h\nu_{365\ nm} \times \text{Ø}_{PL}]$, where ΔI_{SC} (2.85×10^{-4} A at 1.08 mg mL^{-1}) represents the short-circuit current of the Si PV strip offset by the zero-concentration value and measured under 365 nm LED illumination, q (1.6×10^{-19} C) is the elementary charge, Ø_{PV} (about 0.90) is the quantum efficiency of the Si PV strip at 690 nm that is the SiQD fluorescence peak wavelength, I_{light} (2.214 mW cm^{-2}) is the 365 nm LED light intensity, ${W_{LSC}}^2$ (4 cm × 4 cm, Figure 1A) is the light absorbing area, A_{SiQD} (61.71% at 1.08 mg mL^{-1}, Figure 2C) is the absorption of the SiQDs at 365 nm, $h\nu_{365\ nm}$ (5.44×10^{-19} J) is the 365 nm photon energy, and Ø_{PL} (38.86%, Supporting Information, Figure S2) is the PLQY of the SiQD suspension at 365 nm. When the SiQD concentration is at 1.08 mg mL^{-1}, the η_{opt} of the SiQD-LSC is estimated to be 50.66%, which is similar to the SiQD-LSC fabricated previously.[27] In comparison, the maximum theoretical value of the η_{opt} defined by the Snell's law is $(1 - {n_{air}}^2/{n_{ODE}}^2)^{1/2} = 72\%$, where $n_{air} = 1$ and $n_{ODE} = 1.44$ (Supporting Information, Figure S7). The optical loss can be attributed to the SiQD reabsorption and the absorption and scattering due to the nonideal waveguiding structures of the SiQD-LSC. On the other hand, if considering the percentage of the incident excitation photons being converted to the SiQD fluorescence photons received by the Si PV strip, the external optical efficiency, $\eta_{opt,\ external} = [4 \times \Delta I_{SC}/q/\text{Ø}_{PV}]/[I_{light} \times {W_{LSC}}^2/h\nu_{365\ nm}]$, becomes 12.15%.

When the air gap is eliminated and a thin layer of immersion lens oil (refractive index = 1.52) is placed between the SiQD-LSC and PSC, the SiQD-LSC is not thoroughly surrounded by air, and therefore, the η_{opt} of the SiQD-LSC drops significantly from 50.66% to 12.73%, indicating that the SiQD fluorescence photons, except the front-surface escape cone loss, tend to propagate to the PSC rather than the Si PV strip. In this case, the SiQD-LSC acts more like a luminescent downshifter than a concentrator. As a result, the EQEs and PCEs of the SiQD-LSC with no air gap (Figure 4A,D) become much smaller than the SiQD-LSC with the air gap (Figure 3A,D). For instance, the 365 nm EQE decreases from 10.94% at 1.08 mg mL^{-1} to 2.75%, and the PCE decreases from 0.13% at 4.32 mg mL^{-1} to 0.02%. On the other hand, the EQEs and PCEs of the PSC with no air gap (Figure 4B,E) slightly improve over the PSC with the air gap (Figure 3B,E). Most importantly, for the SiQD concentrations from zero to 1.08 mg mL^{-1}, the 465 and 525 nm EQEs of the SiQD-LSC/PSC tandem solar cell exhibit up to 4.6% and up to 5.0% enhancement over the bare PSC, respectively, while the PCE achieves up to 6.2% enhancement compared to the bare PSC (Figure 4C,F and Supporting Information, Table S2). This result is very different from the previous case with the air gap for which the combined EQEs are higher than the bare PSC only at high SiQD concentrations and the combined PCEs are always lower than the bare PSC (Figure 3C,F and Supporting Information, Table S2). The air gap, although enabling the waveguiding ability of the SiQD-LSC, introduces another reflection at the PSC front surface, which basically cancels out the enhancement brought by the nanoporous PMMA ARC at the SiQD-LSC front surface. Lastly, at 1.08 mg mL^{-1}, although the SiQD-LSC/PSC tandem solar cell achieves almost the same PCE as the bare PSC (red circle in Figure 4F), the front SiQD-LSC in the tandem structure absorbs 69% of the solar UV (red circle in Figure 2D), making the back PSC more stable than the bare PSC. Under continuous 2 sun irradiation for 8 h, the back PSC of the SiQD-LSC/PSC tandem solar cell was able to maintain about 85% of the initial PCE, while the bare PSC only retained about 55% of the initial PCE under the same testing condition (Supporting Information, Figure S8).

In addition to the 365, 465, and 525 nm EQE analysis at different SiQD concentrations, the EQE spectra (from 300 to 900 nm) of the front SiQD-LSC, the back PSC, and the combination of both at constant SiQD concentration (1.08 mg mL^{-1}) are characterized (Supporting Information, Figure S9). It is worth noticing that since the monochromatic light spot size (0.5 cm × 0.5 cm) is smaller than the light absorbing area of the SiQD-LSC and PSC (4 cm × 4 cm), the EQEs of the SiQD-LSC and PSC are generally smaller than those measured with the whole light absorbing area illuminated as shown in Figures 3A−C and 4A−C. For the SiQD-LSC, such phenomenon should be attributed to the reabsorption of the SiQD fluorescence, while for the PSC, the unilluminated subcells may lead to high series resistance, making the extraction of photocurrent more difficult. Furthermore, the short-circuit currents calculated by integrating the EQE spectra with the AM1.5G photon flux spectrum are comparable to the measured short-circuit currents as shown in Table S1 (Supporting Information, Figure S10). With a 1 mm air gap between the SiQD-LSC and PSC (Supporting Information, Figure S9A−C), from 300 to 400 nm, owing to the large EQE contribution from the SiQD-LSC, the EQE of the SiQD-LSC/PSC tandem solar cell is obviously higher than the bare PSC, which is consistent with the results in Figure 3C. However, from 400 to 700 nm, due to the significantly decreased EQE of the SiQD-LSC and the extra two reflections at the LSC/air and air/PSC interfaces, the EQE of the SiQD-LSC/PSC tandem solar cell becomes smaller compared to the bare PSC. Furthermore, since the EQE of the SiQD-LSC/PSC tandem solar cell is higher than the bare PSC only in the UV range but lower in most other wavelength ranges, the overall PCE of the SiQD-LSC/PSC tandem solar cell is lower than the bare PSC (red circle in Figure 3F). In contrast, when there is no air gap between the SiQD-LSC and PSC (Supporting Information, Figure S9D−F), since the waveguiding ability of the SiQD-LSC diminishes, making the EQE contribution from the SiQD-LSC negligible, the EQE of the SiQD-LSC/PSC tandem solar cell is smaller than the bare PSC from 340 to 540 nm, which is similar to the results in Figure 4C. However, from 540 to 800 nm, due to the enhancement from the nanoporous PMMA ARC, the EQE of the SiQD-LSC/PSC tandem solar cell is higher than the bare PSC. Lastly, since the EQE enhancement from 540 to 800 nm compensates the EQE degradation from 340 to 540 nm, the overall PCE of the SiQD-LSC/PSC

https://doi.org/10.1021/acsphotonics.1c00550
ACS Photonics 2021, 8, 2392−2399

tandem solar cell is about the same as the bare PSC (red circle in Figure 4F).

CONCLUSION

In this work, we demonstrate a four-terminal tandem solar cell consisting of a LSC filled with colloidal SiQDs in front of a 4 cm × 4 cm PSC. The SiQD-LSC front surface is uniformly covered with a nanoporous PMMA ARC which enhances the transmission by up to 3% from visible to near-infrared range. The SiQD suspension in ODE inside the LSC primarily absorbs the UV portion of the solar irradiation, re-emitting red fluorescence with the peak wavelength located at 690 nm and the 365 nm PLQY equal to 38.86%. The SiQD fluorescence propagates across the planar waveguiding structure to the edges, where the concentrated fluorescence is converted to electricity by a conventional Si PV strip. After passing through the front SiQD-LSC which absorbs the UV part, the rest of the incident sunlight is absorbed by the back PSC. With an air gap between the SiQD-LSC and PSC, compared to the bare PSC, the SiQD-LSC/PSC tandem solar cell can achieve higher 365, 465, and 525 nm EQEs at high SiQD concentrations. Particularly, the 365 nm EQE has a peak equal to 15.36% at 1.08 mg mL^{-1}, corresponding to 47% enhancement over the bare PSC. However, the PCEs of the SiQD-LSC/PSC tandem solar cell are lower than the bare PSC for all SiQD concentrations. In contrast, when the air gap is removed, the optical efficiency of the SiQD-LSC drops significantly from 50.66% to 12.73%, indicating that the SiQD fluorescence photons, except the front-surface escape cone loss, tend to propagate to the back PSC rather than the Si PV strip. In this case, the SiQD-LSC becomes a luminescent downshifter than a concentrator, and the SiQD-LSC/PSC tandem solar cell exhibits up to 4.6% 465 nm EQE enhancement, up to 5.0% 525 nm EQE enhancement and up to 6.2% PCE enhancement over the bare PSC at low SiQD concentrations. Particularly, at 1.08 mg mL^{-1}, although the tandem solar cell has about the same PCE as the bare PSC, the front SiQD-LSC absorbs 69% of the solar UV, making the back PSC more stable than the bare PSC. Under continuous 2 sun irradiation for 8 h, the back PSC of the SiQD-LSC/PSC tandem solar cell was able to maintain about 85% of the initial PCE, while the bare PSC only retained about 55% of the initial PCE under the same testing condition.

ASSOCIATED CONTENT

Supporting Information

The Supporting Information is available free of charge at https://pubs.acs.org/doi/10.1021/acsphotonics.1c00550.

FFT electron diffraction pattern and interplanar spacing of the SiQD; spectra for calculating the PLQY of the SiQD suspension; complex refractive index of the nanoporous PMMA ARC on the quartz slab; spectra of the AM1.5G solar spectrum multiplied by the transmission spectra of the SiQD-LSC with different SiQD concentrations; photographs and IV characteristics of the PSC and Si PV strip; escape cone loss analysis of the SiQD-LSC; stability analysis for the bare PSC and the back PSC of the SiQD-LSC/PSC tandem solar cell; EQE spectra of the front SiQD-LSC, the back PSC, and the combination of both from 300 to 900 nm; values of the short-circuit current, open-circuit voltage, and fill factor of the SiQD-LSC and PSC under xenon arc lamp illumination at different SiQD concentrations; and values of the 365, 465, and 525 nm EQEs and the PCE of the SiQD-LSC/PSC tandem solar cell at different SiQD concentrations (PDF)

AUTHOR INFORMATION

Corresponding Authors

Chang-Ching Tu − *University of Michigan-Shanghai Jiao Tong University Joint Institute, Shanghai Jiao Tong University, Shanghai 200240, China;* orcid.org/0000-0002-9233-1928; Phone: +86-21-34206765; Email: changching.tu@sjtu.edu.cn

Yunlong Guo − *University of Michigan-Shanghai Jiao Tong University Joint Institute, Shanghai Jiao Tong University, Shanghai 200240, China*; Phone: +86-21-34206765; Email: yunlong.guo@sjtu.edu.cn

Songwang Yang − *CAS Key Laboratory of Materials for Energy Conversion, Shanghai Institute of Ceramics, Chinese Academy of Sciences, Shanghai 201899, China;* orcid.org/0000-0001-6304-5941; Phone: +86-21-52412352; Email: swyang@mail.sic.ac.cn

Authors

Shuzhen Ren − *University of Michigan-Shanghai Jiao Tong University Joint Institute, Shanghai Jiao Tong University, Shanghai 200240, China*

Chunhui Shou − *Zhejiang Energy Group R&D Institute Co., Ltd. and Key Laboratory of Solar Energy Utilization & Energy Saving Technology of Zhejiang Province, Zhejiang 311121, China*

Shengli Jin − *Zhejiang Energy Group R&D Institute Co., Ltd. and Key Laboratory of Solar Energy Utilization & Energy Saving Technology of Zhejiang Province, Zhejiang 311121, China*

Guo Chen − *University of Michigan-Shanghai Jiao Tong University Joint Institute, Shanghai Jiao Tong University, Shanghai 200240, China*

Shanshan Han − *University of Michigan-Shanghai Jiao Tong University Joint Institute, Shanghai Jiao Tong University, Shanghai 200240, China*

Zongqi Chen − *CAS Key Laboratory of Materials for Energy Conversion, Shanghai Institute of Ceramics, Chinese Academy of Sciences, Shanghai 201899, China*

Xinyu Chen − *CAS Key Laboratory of Materials for Energy Conversion, Shanghai Institute of Ceramics, Chinese Academy of Sciences, Shanghai 201899, China*

Complete contact information is available at: https://pubs.acs.org/10.1021/acsphotonics.1c00550

Notes

The authors declare no competing financial interest.

ACKNOWLEDGMENTS

This research was financially supported by the Zhejiang Energy Group R&D Institute Co., Ltd. (JSYJY-JS-2019-014) and Shanghai Talent Development Foundation (Grant No. 2018039).

REFERENCES

(1) Kojima, A.; Teshima, K.; Shirai, Y.; Miyasaka, T. Organometal Halide Perovskites as Visible-Light Sensitizers for Photovoltaic Cells. *J. Am. Chem. Soc.* **2009**, *131*, 6050−6051.

(2) NREL Best Research-Cell Efficiency Chart (https://www.nrel.gov/pv/cell-efficiency.html).
(3) Meng, L.; You, J.; Yang, Y. Addressing the Stability Issue of Perovskite Solar Cells for Commercial Applications. *Nat. Commun.* **2018**, *9*, 5265.
(4) Song, Z.; McElvany, C. L.; Phillips, A. B.; Celik, I.; Krantz, P. W.; Watthage, S. C.; Liyanage, G. K.; Apul, D.; Heben, M. J. A Technoeconomic Analysis of Perovskite Solar Module Manufacturing with Low-Cost Materials and Techniques. *Energy Environ. Sci.* **2017**, *10*, 1297−1305.
(5) Rong, Y.; Hu, Y.; Mei, A.; Tan, H.; Saidaminov, M. I.; Seok, S. I.; McGehee, M. D.; Sargent, E. H.; Han, H. Challenges for Commercializing Perovskite Solar Cells. *Science* **2018**, *361*, eaat8235.
(6) Futscher, M. H.; Lee, J. M.; McGovern, L.; Muscarella, L. A.; Wang, T.; Haider, M. I.; Fakharuddin, A.; Schmidt-Mende, L.; Ehrler, B. Quantification of Ion Migration in $CH_3NH_3PbI_3$ Perovskite Solar Cells by Transient Capacitance Measurements. *Mater. Horiz.* **2019**, *6*, 1497−1503.
(7) Yang, J.; Siempelkamp, B. D.; Liu, D.; Kelly, T. L. Investigation of $CH_3NH_3PbI_3$ Degradation Rates and Mechanisms in Controlled Humidity Environments Using *in Situ* Techniques. *ACS Nano* **2015**, *9*, 1955−1963.
(8) Conings, B.; Drijkoningen, J.; Gauquelin, N.; Babayigit, A.; D'Haen, J.; D'Olieslaeger, L.; Ethirajan, A.; Verbeeck, J.; Manca, J.; Mosconi, E.; Angelis, F. D.; Boyen, H.-G. Intrinsic Thermal Instability of Methylammonium Lead Trihalide Perovskite. *Adv. Energy Mater.* **2015**, *5*, 1500477.
(9) Chen, T.-P.; Lin, C.-W.; Li, S.-S.; Tsai, Y.-H.; Wen, C.-Y.; Lin, W. J.; Hsiao, F.-M.; Chiu, Y.-P.; Tsukagoshi, K.; Osada, M.; Sasaki, T.; Chen, C.-W. Self-Assembly Atomic Stacking Transport Layer of 2D Layered Titania for Perovskite Solar Cells with Extended UV Stability. *Adv. Energy Mater.* **2018**, *8*, 1701722.
(10) Leijtens, T.; Eperon, G. E.; Pathak, S.; Abate, A.; Lee, M. M.; Snaith, H. J. Overcoming Ultraviolet Light Instability of Sensitized TiO_2 with Meso-Superstructured Organometal Tri-Halide Perovskite Solar Cells. *Nat. Commun.* **2013**, *4*, 2885.
(11) Arora, N.; Dar, M. I.; Hinderhofer, A.; Pellet, N.; Schreiber, F.; Zakeeruddin, S. M.; Gratzel, M. Perovskite Solar Cells with CuSCN Hole Extraction Layers Yield Stabilized Efficiencies Greater Than 20%. *Science* **2017**, *358*, 768−771.
(12) Hou, Y.; Du, X.; Scheiner, S.; McMeekin, D. P.; Wang, Z.; Li, N.; Killian, M. S.; Chen, H.; Richter, M.; Levchuk, I.; Schrenker, N.; Spiecker, E.; Stubhan, T.; Luechinger, N. A.; Hirsch, A.; Schmuki, P.; Steinrück, H.-P.; Fink, R. H.; Halik, M.; Snaith, H. J.; Brabec, C. J. A Generic Interface to Reduce the Efficiency-Stability-Cost Gap of Perovskite Solar Cells. *Science* **2017**, *358*, 1192−1197.
(13) Tan, H.; Jain, A.; Voznyy, O.; Lan, X.; Garcia de Arquer, F. P.; Fan, J. Z.; Quintero-Bermudez, R.; Yuan, M.; Zhang, B.; Zhao, Y.; Fan, F.; Li, P.; Quan, L. N.; Zhao, Y.; Lu, Z.-H.; Yang, Z.; Hoogland, S.; Sargent, E. H. Efficient and Stable Solution-Processed Planar Perovskite Solar Cells via Contact Passivation. *Science* **2017**, *355*, 722−726.
(14) Idígoras, J.; Aparicio, F. J.; Contreras-Bernal, L.; Ramos-Terrón, S.; Alcaire, M.; Sánchez-Valencia, J. R.; Borras, A.; Barranco, Á.; Anta, J. A. Enhancing Moisture and Water Resistance in Perovskite Solar Cells by Encapsulation with Ultrathin Plasma Polymers. *ACS Appl. Mater. Interfaces* **2018**, *10*, 11587−11594.
(15) Kim, H.; Lee, J.; Kim, B.; Byun, H. R.; Kim, S. H.; Oh, H. M.; Baik, S.; Jeong, M. S. Enhanced Stability of MAPbI3 Perovskite Solar Cells using Poly(p-chloro-xylylene) Encapsulation. *Sci. Rep.* **2019**, *9*, 15461.
(16) Jiang, L.; Chen, W.; Zheng, J.; Zhu, L.; Mo, L.; Li, Z.; Hu, L.; Hayat, T.; Alsaedi, A.; Zhang, C.; Dai, S. Enhancing the Photovoltaic Performance of Perovskite Solar Cells with a Down-Conversion Eu-Complex. *ACS Appl. Mater. Interfaces* **2017**, *9*, 26958−26964.
(17) Jia, J.; Dong, J.; Lin, J.; Lan, Z.; Fan, L.; Wu, J. Improved Photovoltaic Performance of Perovskite Solar Cells by Utilizing Down-Conversion $NaYF_4:Eu^{3+}$ Nanophosphors. *J. Mater. Chem. C* **2019**, *7*, 937−942.
(18) Jin, J.; Chen, C.; Li, H.; Cheng, Y.; Xu, L.; Dong, B.; Song, H.; Dai, Q. Enhanced Performance and Photostability of Perovskite Solar Cells by Introduction of Fluorescent Carbon Dots. *ACS Appl. Mater. Interfaces* **2017**, *9*, 14518−14524.
(19) Tao, R.; Fang, W.; Li, F.; Sun, Z.; Xu, L. Lanthanide-Containing Polyoxometalate as Luminescent Down-Conversion material for improved printable perovskite solar cells. *J. Alloys Compd.* **2020**, *823*, 153738.
(20) Macdonald, D.; Cuevas, A.; Kerr, M. J.; Samundsett, C.; Ruby, D.; Winderbaum, S.; Leo, A. Texturing industrial multicrystalline silicon solar cells. *Sol. Energy* **2004**, *76*, 277−283.
(21) Chandra Sekhar Reddy, K.; Karthik, D.; Bhanupriya, D.; Ganesh, K.; Ramakrishna, M.; Sakthivel, S. Broad band antireflective coatings using novel in-situ synthesis of hollow MgF_2 nanoparticles. *Sol. Energy Mater. Sol. Cells* **2018**, *176*, 259−265.
(22) Li, J.; Lu, Y.; Lan, P.; Zhang, X.; Xu, W.; Tan, R.; Song, W.; Choy, K.-L. Design, preparation, and durability of TiO_2/SiO_2 and ZrO_2/SiO_2 double-layer antireflective coatings in crystalline silicon solar modules. *Sol. Energy* **2013**, *89*, 134−142.
(23) Sarkın, A. S.; Ekren, N.; Sağlam, Ş. A review of anti-reflection and self-cleaning coatings on photovoltaic panels. *Sol. Energy* **2020**, *199*, 63−73.
(24) Thangavel, N. R.; Adhyaksa, G. W. P.; Dewi, H. A.; Tjahjana, L.; Bruno, A.; Birowosuto, M. D.; Wang, H.; Mathews, N.; Mhaisalkar, S. Disordered polymer antireflective coating for improved perovskite photovoltaics. *ACS Photonics* **2020**, *7*, 1971−1977.
(25) Jošt, M.; Kegelmann, L.; Korte, L.; Albrecht, S. Monolithic perovskite tandem solar cells: a review of the present status and advanced characterization methods toward 30% efficiency. *Adv. Energy Mater.* **2020**, *10*, 1904102.
(26) Li, H.; Zhang, W. Perovskite tandem solar cells: from fundamentals to commercial deployment. *Chem. Rev.* **2020**, *120*, 9835−9950.
(27) Han, S.; Chen, G.; Shou, C.; Peng, H.; Jin, S.; Tu, C.-C. Visibly transparent solar windows based on colloidal silicon quantum dots and front-facing silicon photovoltaic cells. *ACS Appl. Mater. Interfaces* **2020**, *12*, 43771−43777.
(28) Guo, Y.; Ren, S. Bilayer PMMA antireflective coatings via microphase separation and MAPLE. *J. Polym. Eng.* **2021**, *41*, 164−173.
(29) Meinardi, F.; McDaniel, H.; Carulli, F.; Colombo, A.; Velizhanin, K. A.; Makarov, N. S.; Simonutti, R.; Klimov, V. I.; Brovelli, S. Highly Efficient Large-Area Colourless Luminescent Solar Concentrators Using Heavy-Metal-Free Colloidal Quantum Dots. *Nat. Nanotechnol.* **2015**, *10*, 878−885.

https://doi.org/10.1021/acsphotonics.1c00550
ACS Photonics 2021, 8, 2392−2399